Proposal for quantum memory miniaturization in superconducting circuit QED

Genting Dai [1,*] Kaiyong He [1] Yongcheng He [1] Changhao Zhao,[1] Jianshe Liu [1] and Wei Chen [1,2,3,†]

[1]*Laboratory of Superconducting Quantum Information Processing, School of Integrated Circuits, Tsinghua University, Beijing 100084, China*
[2]*Beijing National Research Center for Information Science and Technology, Beijing 100084, China*
[3]*Beijing Innovation Center for Future Chips, Tsinghua University, Beijing 100084, China*

Superconducting circuit quantum electrodynamics is the main architecture for implementation of quantum processors. This work presents a proposal to miniaturize quantum memory devices by combining the quantum memory qubits encoded directly in the first two Fock states $\{|0\rangle, |1\rangle\}$ and the bus channel in the same specially designed multimode cavity. One key feature of the resonant modes used for quantum memory is that the microwave current is localized, which facilitates the storage and retrieval of information in superconducting qubits while preventing crosstalk from other resonant modes. Frequency design and distinct coupling strengths in this kind of device are analyzed with electromagnetic simulations and numerical calculations. The quantum memory properties, e.g., storage speed, fidelity, and stability, are examined in four cases: (1) memory operation of single-qubit state, (2) disturbing effects, (3) coupling operation, and (4) entangled states storage. Decoherence time of the quantum processor can be extended to more than one order of magnitude longer than that without the memory. By integrating transmons with optimally designed coplanar waveguide multimode quantum memories, the present study could provide an optimistic perspective for the development of large-scale superconducting quantum processors.

I. INTRODUCTION

The architecture based on circuit quantum electrodynamics (QED) is a leading platform in the research and development of scalable superconducting quantum processors [1–9]. Some vital work in this field has been reported, such as benchmarking Floquet quantum simulation with superconducting qubits [5], using superconducting processors to sample the output of a pseudorandom quantum circuit [6], and taking random quantum circuit sampling [9]. The superconducting circuits consisting of transmon qubits based on Josephson junctions usually rely on a coplanar waveguide (CPW) bus or nearest-neighbor interactions for coupling operations. The transmon qubits are able to provide excellent controllability of the quantum state and fast quantum gates [10]. To pursuit gate operations with high fidelity and place superconducting circuits closer to the threshold of quantum error corrections, the task of improving the coherence time of the superconducting quantum processors stands out as an imperative issue.

In order to prolong the coherence time of superconducting processors, two main strategies have been proposed. The first is to optimize qubits directly because the superconducting qubits are expensive in terms of control resources and struggle with the relatively short coherence time [11]. It has been demonstrated that the decoherence time of these optimized qubits can exceed 0.3–0.5 ms [12,13], though not much work has been published about realizing quantum gates with these optimized qubits. The other promising strategy is utilizing quantum memory, which is regarded as a key element of quantum computing systems [14–17]. There are many kinds of physical systems available for acting as quantum memory in the superconducting circuit QED system, including nitrogen vacancy (NV) centers [18–20], magnetic particles [21], 3D cavity [22,23], CPW resonators [17,24,25], and so on. For the first two physical systems, a hybrid system could combine the advantages of every subsystem, while it would increase the complexity of quantum operations. For the microwave resonator including 3D cavity and CPW with a high-quality factor, they are natural and viable choices for storing microwave photons [14,16,22,26–31], which are able to have strong coupling with the superconducting qubits and form an effective quantum interface between the photons and the qubits [11,17].

The 3D cavity can reach a high-quality factor and provide long decoherence time [22,30]. It is limited by the scalability, which would lead to less effective resonant modes and more difficulties in storing a great deal of quantum information [10]. For the cavity working as quantum memory, three basic requirements arise: (1) a sufficient number of resonant modes, (2) enough coupling strength to transfer the quantum state with high speed, and (3) mode frequencies matched to superconducting qubits. Memory qubits should have longer coherence time than the transmons in the same system for more than one order of magnitude, but are incapable of logic operations directly [11]. With careful design in the Schrödinger cat state based on a superposition of coherent states, it is possible to use resonant modes in the CPW cavity as memory qubits [28]. To get a long coherence time for the

*dgt20@mails.tsinghua.edu.cn
†weichen@tsinghua.edu.cn

CPW memory qubits, the internal quality factors should be boosted. It can be achieved over 10^6 via careful fabrication to minimize the occurrence of two-level systems and by the etching techniques to reduce substrate-vacuum interfaces in the region of high electric fields [10,32]. Many schematics for connecting superconducting qubits to a number of memory qubits with superior coherence have been proposed [11,17,22,25,33,34]. However, extra CPW resonators to be used in quantum processors for storage would take up many footprints on the superconducting quantum chip.

In this work a proposal to construct a miniaturized and integrated quantum memory encoded with Fock states $\{|0\rangle, |1\rangle\}$ is presented based on a superconducting multiple-branch multimode cavity, where the quantum memory cavity is combined with the bus cavity in a circuit QED system. The scheme is aimed at prolonging the decoherence time of quantum processor and reducing the total size of the CPW used on chip. Electromagnetic simulation of the current distributions reveals two kinds of resonant modes in the specially designed multimode cavity to realize the quantum memory and bus channel together. For higher selectivity of these resonant modes and realizing memory operations between the transmon and memory qubit with high fidelity, different coupling strengths utilized in the structure are determined based on the calculated results of state fidelity and photon number in the memory qubit. Performance of the quantum memory is examined in four cases.

The paper is organized as follows. In Sec. II the model of the multimode cavity and the simulated results are presented. A conceptual quantum memory based on the multiple-branch multimode cavity is given in Sec. III, including frequency design in the system. In Sec. IV the protocol for memory operations and coupling operations is demonstrated. Four different situations are examined to characterize the properties of the quantum memory, including storage speed, storage fidelity, and stability. In Sec. V comparisons of other quantum memory protocols with this work and relative issues are discussed, followed by the conclusion and summary in Sec. VI.

II. MODEL AND ANALYSIS

A. Multimode cavity and simulation

To construct a multimode cavity containing resonant modes for two distinct functions, bus channel and quantum memory, a kind of CPW with multiple branches is proposed. The structure diagram is shown in Fig. 1 for a multiple-branch cavity chip. The CPW has four branches originating from the center of the chip. The four branches are classified into two groups by their lengths $l_k, (k = 1, 2)$. Four ports (P_1–P_4) are coupled capacitively to the four ends of the multiple-branch cavity.

The electromagnetic field in the multiple-branch cavity is simulated with SONNET. In Fig. 2 results are shown through the scattering parameter [35] and current distribution in every branch. The lengths of four branches in the cavity are $l_1 = 5$ mm, $l_2 = 8$ mm. Figure 2(a) shows the magnitude of scattering parameters S_{12} (solid blue line) and S_{34} (dot-dashed red line). For S_{12}, there are two transmission peaks $f_2 = 4.86$ GHz, $f_3 = 6.30$ GHz and a absorption peak
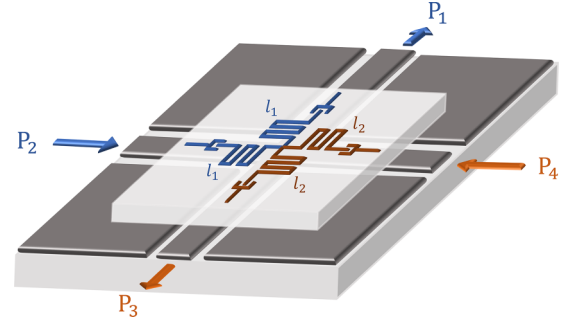

FIG. 1. Structure of the multiple-branch cavity. The CPW has four branches connected to a common node in the center of the chip. The four branches are divided into two groups, which have lengths l_1 and l_2, respectively. The multiple-branch cavity is coupled to the four ports (P_1–P_4) via capacitors.

$f_{a1} \approx 3.95$ GHz. Similarly, for S_{34}, there two transmission peaks $f_1 = 3.97$ GHz, $f_2 = 4.86$ GHz and a absorption peak $f_{a2} \approx 6.24$ GHz. It can be seen clearly that the parameters of S_{12} and S_{34} share a transmission peak at $f_2 = 4.86$ GHz. The quality factor of these resonant modes is estimated to be about 2×10^4.

Figure 2(b) gives the diagrammatic layout of the multiple-branch cavity. The width of the central conductor in the CPW is 10 μm, and the width of the waveguide gap is 6 μm. In reference to it, the current distribution of three transmission peaks f_1, f_2, and f_3 is displayed in Figs. 2(c)–2(e), respectively. The current is localized almost only in the two branches with length $l_2 = 8$ mm at microwave signal $f_1 = 3.97$ GHz; see Fig. 2(c). Similarly, in Fig. 2(e) the current is contained in the two branches with length $l_1 = 5$ mm at microwave signal $f_3 = 6.30$ GHz. These two local modes are denoted as special resonant modes in this work. In contrast to these special modes, when the microwave signal is at $f_2 = 4.86$ GHz, the current flows in all the four branches of the cavity symmetrically. Naturally, this mode is called the common mode in this work.

According to the simulated results, there are three resonant modes in this cavity. The three resonant modes can be divided into two kinds of resonant modes. The first one is the common resonant mode, which is accessible to all four ports and is suitable to be used as the bus channel [25,36–42]. The other is the special resonant mode, which exists in the specific location of the multimode cavity with a high magnitude of transmission and relatively high-quality factor. Therefore, it has the potential to be used as a superconducting quantum memory qubit.

The above simulation results can be interpreted intuitively by a simple calculation. For a resonator with two branches of equal length $l_k (k = 1, 2)$, the resonant frequency satisfies

$$f_k = \frac{c}{4l_k\sqrt{\varepsilon_{\text{eff}}}} \quad (k = 1, 2), \tag{1}$$

where c is the velocity of light in vacuum, and ε_{eff} is the effective permittivity of surrounding material (substrate is sapphire [43,44]).

For the multimode cavity with four branches of length l_1 and l_2 in this work, the three resonant frequencies can be
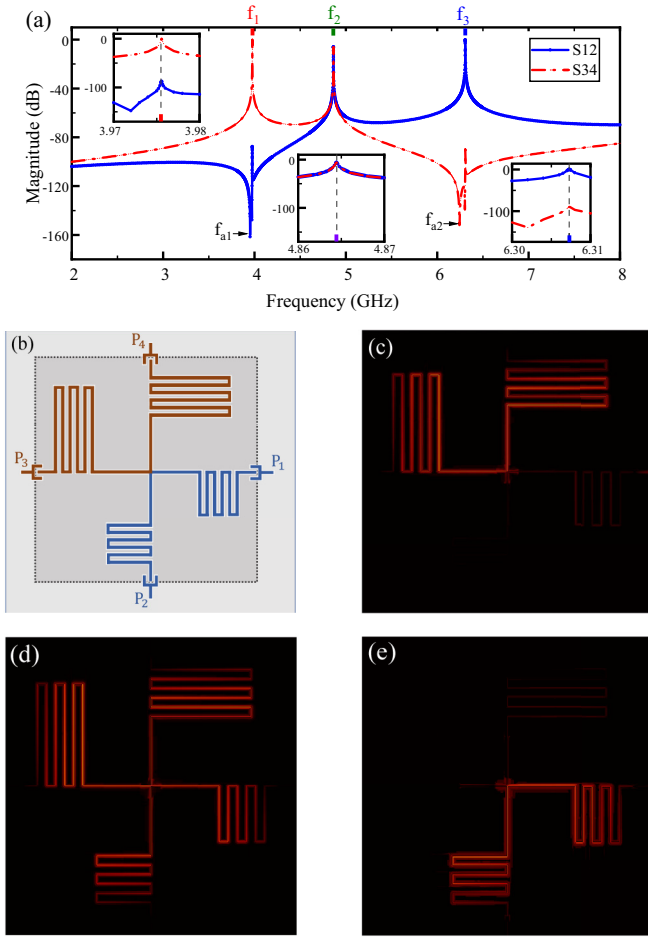
FIG. 2. Electromagnetic simulation results of the multimode cavity. (a) Magnitude of scattering parameters S_{12} (solid blue line) and S_{34} (dot-dashed red line). (b) Diagrammatic layout of the cavity. $l_1 = 5$ mm, $l_2 = 8$ mm. Current distributions in the cavity at microwave signals (c) $f_1 = 3.97$ GHz, (d) $f_2 = 4.86$ GHz, and (e) $f_3 = 6.30$ GHz.

calculated as $f_1^{\text{cal}} = 3.98$ GHz, $f_2^{\text{cal}} = 4.90$ GHz, and $f_3^{\text{cal}} = 6.37$ GHz decided by $2l_2$, $(l_1 + l_2)$ and $2l_1$, respectively. It can be seen that the calculated frequencies f_1^{cal}, f_2^{cal}, and f_3^{cal} are nearly equal to the corresponding simulated frequencies f_1, f_2 and f_3 for an optimal choice of $\varepsilon_{\text{eff}} = 5.55$. Based on the agreement between numerical simulation and analytical calculation, in the multiple-branch cavity, the number of resonant modes can be decided by the number of branches, while the frequencies of modes are related to the length of branches and affected by the length ratio of different branches.

There are three resonant modes in this multimode cavity at the same time. Possible crosstalk among these resonant modes is analyzed through the quantization of the electromagnetic field. For clarity, the angular frequency ω_{jn} denotes the nth-order mode belonging to the jth resonator with length L_j. It is assumed for simplicity that $\omega_{jn} \gg \kappa_{jn}$ ($j = 1, 2, 3; n = 1, 2, 3, \ldots$), where κ_{jn} is the decay rate of the corresponding resonant mode with ω_{jn}. We set up the direction of field propagation as the z direction, and the electric field is polarized in the x direction. The electric field $\mathbb{E}_{jx}$ and the magnetic field

$\mathbb{H}_{jy}$ in the cavity resonator with length L_j can be written as [45,46]

$$\mathbb{E}_{jx}(z, t) = \sum_n A_{jn} q_{jn}(t) \sin(k_{jn}z), \tag{2a}$$

$$\mathbb{H}_{jy}(z, t) = \sum_n A_{jn} \frac{\dot{q}_{jn}(t)\varepsilon_m}{k_{jn}} \cos(k_{jn}z), \tag{2b}$$

where $k_{jn} = n\pi/L_j$, $A_{jn} = \sqrt{2\omega_{jn}^2 m_n/(V_j \varepsilon_m)}$, m_n is a constant with dimension of mass, and ε_m is the permittivity of the superconducting CPW. The resonator has an effective volume of $V_j = L_j A_{\text{eff}}$, where A_{eff} is an effective area of the CPW resonator. The normal mode amplitude q_{jn} has a dimension of length. Furthermore, the eigenfrequency of the cavity is $\omega_{jn} = n\pi v/L_j$, where v is the velocity of light in the medium.

Following the descriptions of Ref. [46], the quantized electric field $\hat{\mathbb{E}}_{1x}$ and magnetic field $\hat{\mathbb{H}}_{1y}$ of the resonator with length L_1 can be written as

$$\hat{\mathbb{E}}_{1x}(z, t) = \sum_n \mathcal{A}_{1n}(\hat{a}_{1n}e^{-i\omega_{1n}t} + \hat{a}_{1n}^\dagger e^{i\omega_{1n}t})\sin(k_{1n}z), \tag{3a}$$

$$\hat{\mathbb{H}}_{1y}(z, t) = -i\varepsilon_m v \sum_n \mathcal{A}_{1n}(\hat{a}_{1n}e^{-i\omega_{1n}t} - \hat{a}_{1n}^\dagger e^{i\omega_{1n}t})\cos(k_{1n}z), \tag{3b}$$

where $\mathcal{A}_{1n} = \sqrt{\hbar\omega_{1n}/(\varepsilon_m V_1)}$. The operators $\hat{a}_{1n}$ and $\hat{a}_{1n}^\dagger$, which satisfy $[\hat{a}_{1n}, \hat{a}_{1n}^\dagger] = 1$, are the annihilation and creation operators, respectively. Similar results can be written for the other two resonators with length L_2 and L_3. Taking any two of them in the multimode cavity ($j = 1$ and $j = 2$), the Hamiltonian of the crosstalk between the two electromagnetic fields can be given as

$$\hat{H}_{\text{cross}} = \frac{1}{2} \int (\varepsilon_m \hat{\mathbb{E}}_{1x}\hat{\mathbb{E}}_{2x} + \mu_m \hat{\mathbb{H}}_{1y}\hat{\mathbb{H}}_{2y}) \, d\tau, \tag{4}$$

where μ_m is the permeability of the medium. A straightforward calculation of Eq. (4) yields a result of zero owing to the orthonormality of the series of trigonometric functions. It suggests that, without consideration of the scattering effect in the system, no crosstalk among photons with different frequencies occurs when they are in the same multimode cavity. Hence it is possible to use these resonant modes in the multimode cavity independently.

B. Hamiltonian

The multiple-branch cavity with two localized special modes (f_1 and f_3) and one common mode (f_2) can function as a multimode cavity with two memory modes ($\omega_1 = 2\pi f_1$ and $\omega_3 = 2\pi f_3$) and one all-connecting bus mode ($\omega_2 = 2\pi f_2$). The conceptual diagram of this kind of superconducting multimode cavity is illustrated in Fig. 3, where the cavity is coupled to four transmon qubits in the dispersive regime of circuit QED [10,47]. The rotation of every qubit on the Bloch sphere is controlled by the XY and Z lines. The Z-control line is also used to adjust the qubit frequency by changing the flux $\Phi(t)$ threading the superconducting quantum interference device (SQUID) of the qubit. The quantum states of each qubit are accessible through the readout chains.
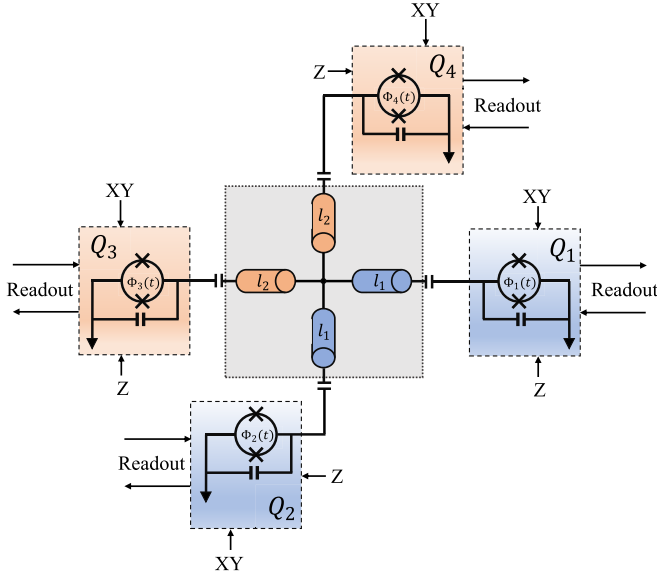
FIG. 3. Conceptual diagram of the superconducting multimode cavity with four transmon qubits Q_i, $(i = 1, 2, 3, 4)$. The qubits are controlled by the XY and Z lines and can be read out separately. The qubit frequencies are tunable via the flux $\Phi(t)$ threading SQUIDs by the Z-control line.

Without consideration of the controlling interaction, the Hamiltonian $\hat{H}$ of the system in Fig. 3 can be written as [48]

$$\hat{H} = \hat{H}_{\mathrm{q}} + \hat{H}_{\mathrm{r}} + \hat{H}_{\mathrm{I}}. \tag{5}$$

Here $\hat{H}_{\mathrm{q}}$ is the Hamiltonian of transmons, $\hat{H}_{\mathrm{r}}$ is the Hamiltonian of the resonators in the multimode cavity, and $\hat{H}_{\mathrm{I}}$ refers to the Hamiltonian of their interactions. The specific formulas for $\hat{H}_{\mathrm{q}}$ is

$$\hat{H}_{\mathrm{q}} = \frac{\hbar}{2} \sum_{i=1}^{4} \Omega_i \hat{\sigma}_i^z, \tag{6}$$

where Ω_i is the resonant frequency of the ith transmon, and $\hat{\sigma}_i^z = |e_i\rangle\langle e_i| - |g_i\rangle\langle g_i|$ is the z Pauli operator of the ith transmon. The Hamiltonian of the multimode cavity is

$$\hat{H}_{\mathrm{r}} = \hbar \sum_{j=1}^{3} \omega_j \left(\hat{a}_j^\dagger \hat{a}_j + \frac{1}{2} \right), \tag{7}$$

where ω_j is the resonant frequency of the jth resonant mode, and $a_j^\dagger (a_j)$ is the creation (annihilation) operator of the jth resonant mode. The Hamiltonian of the interactions between transmons and resonant modes is

$$\hat{H}_{\mathrm{I}} = \hbar \sum_{i,j} g_{ij} (\hat{\sigma}_i^+ \hat{a}_j + \hat{\sigma}_i^- \hat{a}_j^\dagger), \tag{8}$$

where g_{ij} is the coupling strength between the ith transmon and the jth resonant mode, and $\hat{\sigma}_i^+ (\hat{\sigma}_i^-)$ is the raising (lowering) operator of the ith transmon. Substituting Eqs. (6)–(8) into Eq. (5) yields the Jaynes-Cummings Hamiltonian, which is familiar in the circuit QED [48–50].

III. FREQUENCY DESIGN

The frequencies of the fundamental modes in the cavity have been calculated and simulated in Sec. II and can be tuned by the length (l_k) of branches. Comprising a set of resonant frequencies, the multimode circuit QED system is possible to be used as a quantum memory, in which quantum information can be stored and transferred with high connectivity. In order to execute quantum gates to the transmons in the dispersive regime, four qubits should be set up at proper frequencies and coupled to the cavity with appropriate coupling strength [10,48].

Based on the resonant modes in the cavity, the feasible range of qubit frequencies is depicted in Fig. 4(a). According to the simulated results, $\omega_1 = 2\pi \times 3.97$ GHz is the frequency of the first memory mode which exists in the two branches with length $l_2 = 8$ mm. Analogously, the two branches with length $l_1 = 5$ mm host the second memory mode with the frequency $\omega_3 = 2\pi \times 6.30$ GHz. In addition, the bus channel possesses the frequency $\omega_2 = 2\pi \times 4.86$ GHz. The idle frequencies of the four transmon qubits are detuned from the resonant modes more than 500 MHz [51]. The frequency differences $\Delta_{i1} = |\omega_1 - \Omega_i|$, $\Delta_2 = |\omega_2 - \omega_1|$, and $\Delta_3 = |\omega_3 - \omega_2|$ are indicated in Fig. 4(a).

Figure 4(b) illustrates the harmonic potential well of the three resonant modes and cosine potential well of the four transmons. The Fock states $\{|0\rangle, |1\rangle\}$ of the resonant modes are used for encoding the logical states $\{|0_L\rangle, |1_L\rangle\}$ of the memory and bus qubits. The ground state $|g\rangle$ and the first excited state $|e\rangle$ of the transmons are utilized for encoding the logical states $\{|0_L\rangle, |1_L\rangle\}$ of the four transmon qubits [10]. The coupling strength between the ith transmon and the jth resonant mode is denoted by g_{ij}, which satisfies [52]

$$g_{ij} = \sqrt{\Omega_i \omega_j} \frac{C_c}{2\sqrt{(C_{\mathrm{q}} + C_c)(C_{\mathrm{m}} + C_c)}}, \tag{9}$$

where C_c is the coupling capacitance between the transmon qubit and memory qubit, C_q is the capacitance of transmon, and $C_{\mathrm{m}} = 1/(\omega_r Z)$ is the capacitance of the memory qubit.

The coupling strength would effect the speed of information storage and transferring, which can be realized by adjusting the frequencies of transmon qubits. These processes in the multimode circuit QED system are presented in Fig. 5 with a ball-and-stick model [24,53,54]. As shown in Fig. 5(a), the idle frequencies of the transmon qubits are kept lower than that of the bus and memories. Transmons Q_1 and Q_2 share the same memory M_2, while Q_3 and Q_4 enjoy the same memory M_1. All of the transmon qubits get full connectivity with the bus. In Fig. 5(b) the memory operation is carried out by tuning the Q_1 (Q_4) into or near resonance with the M_2 (M_1). Information storage and retraction between transmon qubit and memory qubit is executed by a SWAP gate. The coupling operation via bus is realized by tuning the qubits into resonance, while the qubits are far detuned from the bus mode. Such a coupling operation via bus is utilized to implement a two-qubit gate (e.g., iSWAP) between Q_2 and Q_3.

The ideal time interval $\Delta t|_{\mathrm{ideal}}$ of the SWAP gate is decided by $\Delta t|_{\mathrm{ideal}} = \pi/2g$, in which g is the coupling strength
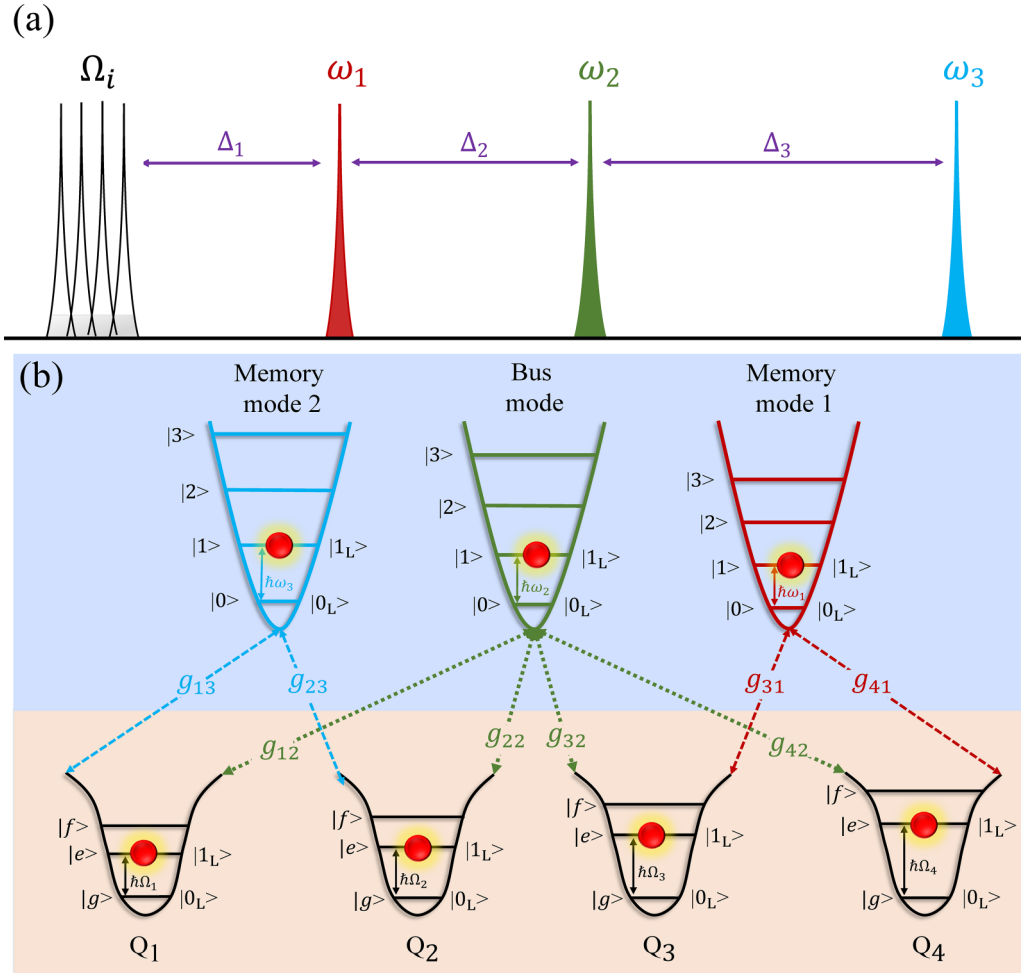
FIG. 4. Frequency design of the multimode circuit QED system. (a) Feasible range of frequency of qubit and resonant modes in the multimode cavity. (b) Energy potential for three resonant modes and four transmons, where the Fock states $|0\rangle$ and $|1\rangle$ are used for encoding the memory and bus qubits. The ground state $|g\rangle$ and the first excited state $|e\rangle$ are utilized for encoding the transmon qubits. The energy levels of the logical $|1_L\rangle$ state of these qubits are marked with red circles, and the lower energy levels are the logical $|0_L\rangle$. The coupling strength between the ith transmon and the jth resonant mode is denoted by g_{ij}.

between two qubits. It suggests that the operation time between two systems is determined by the coupling strength. Moreover, it may affect the precision of operation when there are many resonant modes. Table I lists the circuit parameters and frequencies in the multimode circuit QED system. It should be noted that the qubit-bus coupling strength g_b will be discussed in the next section.

TABLE I. Circuit parameters and frequencies.

Parameter	Symbol	Value
Transmon capacitance	C_q	87.8 fF
M_1 capacitance	C_{m1}	0.802 pF
M_2 capacitance	C_{m2}	0.505 pF
Qubit-memory coupling	$g_m/2\pi$	24 MHz
Qubit-bus coupling	g_b	—
Qubit decay rate [6,9]	γ_i	0.03 MHz
Cavity mode decay rate [32]	κ_j	0.001 MHz

IV. MEMORY PROPERTIES

A quantum memory can generally be characterized by the properties of storage and retraction speed, storage fidelity, and stability. In this section, master equations are utilized to study the effects of various physical factors on the performance of the quantum memory.

The multimode circuit QED system is viewed as an open system, which is composed of transmon qubits, memory qubits, and quantum bus. The evolution process of the density operator $\hat{\rho}$ of the open system is governed by the following master equation [55,56]:

$$\frac{d\hat{\rho}}{dt} = -i[\hat{H}, \hat{\rho}] + \Gamma(2\hat{J}\hat{\rho}\hat{J}^\dagger - \hat{J}^\dagger\hat{J}\hat{\rho} - \hat{\rho}\hat{J}^\dagger\hat{J}) \equiv \mathcal{L}[\hat{\rho}], \quad (10)$$

where $\hat{H}$ is the system Hamiltonian, and $\Gamma > 0$ refers to a rate associated to the jump operator $\hat{J}$ that describes irreversible processes. The Liouvillian superoperator $\mathcal{L}$ acts on the density operator $\hat{\rho}$ of the system. Based on this equation, four different situations are examined as follows.
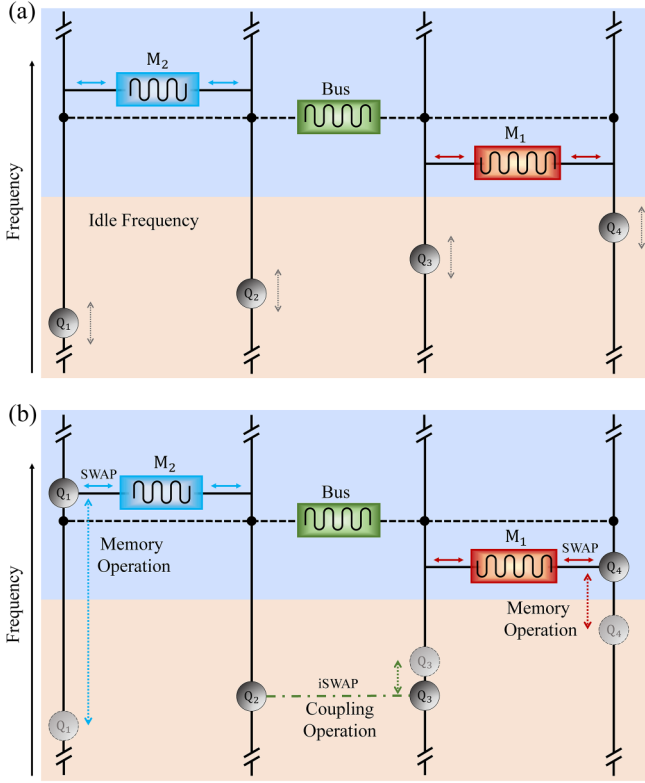
FIG. 5. Ball-and-stick model of the multimode circuit QED system. (a) The frequencies of the multimode cavity (memories M_1, memories M_2, and bus) and the idle frequencies of the transmon qubits. The horizontal double-head arrows on either side of M_1 and M_2 indicate the storage/retraction operation between qubit and memory. (b) Memory and coupling operations via adjusting the frequencies of transmon qubits, indicating by the vertical double-head arrows alongside each transmon qubit. The frequency of Q_1 (Q_4) is tuned into resonance with M_2 (M_1) for a memory operation. The dot-dash line between Q_2 and Q_3 suggests a virtual photon coupling via the bus channel.

A. Coupling strength

Some requirements on coupling strength are proposed when utilizing the memory operation in the multimode circuit QED system. The first case to be studied is the memory operation between Q_3 and M_1. In Fig. 6(a) the ball-and-stick model for Case I is shown, where two transmons Q_3 and Q_4 are coupled to the memory qubit M_1 and the bus channel. The transmon qubit Q_3 is excited and stored into M_1. The Hamiltonian $\hat{H}_{CI}$ for the subsystem in Case I, according to Eqs. (5)–(8), is written as (set $\hbar = 1$)

$$\hat{H}_{CI} = \frac{1}{2}\left(\Omega_3 \hat{\sigma}_3^z + \Omega_4 \hat{\sigma}_4^z\right) + \omega_1 \hat{a}_1^\dagger \hat{a}_1 + \omega_2 \hat{a}_2^\dagger \hat{a}_2$$
$$+ \left(g_{31}\hat{\sigma}_3^+ \hat{a}_1 + g_{41}\hat{\sigma}_4^+ \hat{a}_1 + \text{H.c.}\right)$$
$$+ \left(g_{32}\hat{\sigma}_3^+ \hat{a}_2 + g_{42}\hat{\sigma}_4^+ \hat{a}_2 + \text{H.c.}\right). \quad (11)$$

The transmon Q_3 is excited at $\Omega_3 = 3.1 \times 2\pi$ GHz, while Q_4 is at ground state with $\Omega_4 = 3.2 \times 2\pi$ GHz.

The state fidelity of a quantum system is usually defined as

$$\mathcal{F}_s = \text{Tr}(\hat{\rho}_0 \hat{\rho}) - \sqrt{1 - \text{tr}(\hat{\rho}_0)^2}\sqrt{1 - \text{tr}(\hat{\rho})^2}, \quad (12)$$
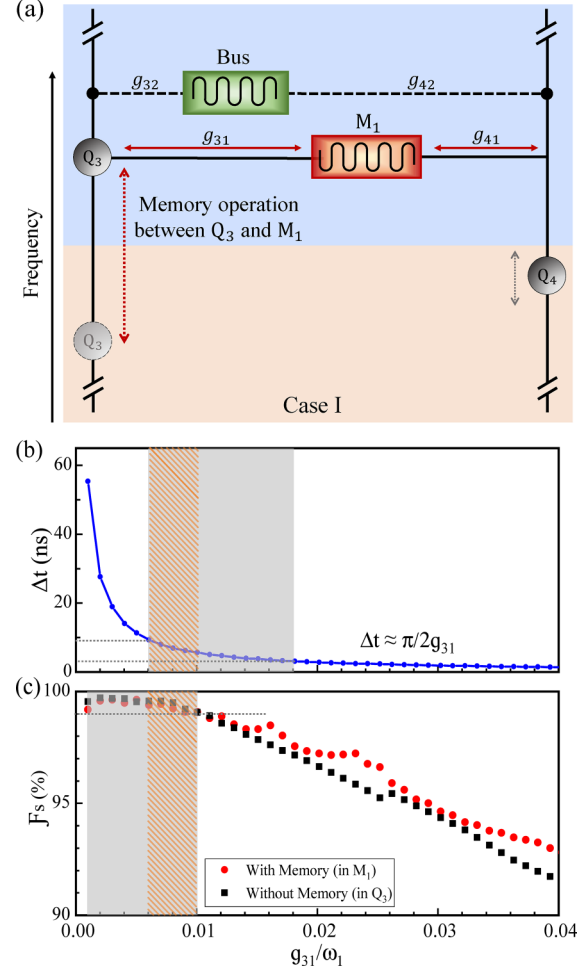

FIG. 6. Model and calculation results of Case I. (a) Ball-and-stick model for Case I: the memory operation between Q_3 and M_1, which are coupled with strength g_{31}. (b) The memory operation time Δt for different amplitude of the coupling strength g. (c) The state fidelity $\mathcal{F}_s$ for different amplitude of coupling strength g_{31}. One group is with memory marked by red scatter circles, the other is without memory marked by black scatter squares.

where $\hat{\rho}_0$ is the initial density matrix and $\hat{\rho}$ is the measured density matrix [57]. In the subsystem of Case I, the initial state is the pure state, and then the state fidelity $\mathcal{F}_s$ can be calculated directly by

$$\mathcal{F}_s = \text{Tr}(\hat{\rho}_0 \hat{\rho}). \quad (13)$$

The frequency of Q_3 is tuned to resonant with M_1 at $t_0 = 0$ ns and lasts for a memory operation time period Δt, which might be a little different from the ideal time interval $\Delta t|_{ideal}$ of the SWAP operation. Figure 6(b) presents the variation of Δt with the coupling strength g_{31} between Q_3 and M_1. It can be seen that the operation time Δt gets shorter with larger coupling strength following the relationship $\Delta t \approx \pi/2g_{31}$. In the gray range of $g_{31}/\omega_1 \in [0.006, 0.018]$, one can get an appropriate operation time $\Delta t \in [3, 10]$ ns.

To find the effects of coupling strength g_{31} on the fidelity, two groups of the state fidelity $\mathcal{F}_s$ are calculated. One group has a memory operation between Q_3 and M_1 starting at $t_0 = 0$ ns, and the $\mathcal{F}_s$ is calculated at $t_1 = \pi/2g_{31}$ ns. The other

group has no memory operation, and the $\mathcal{F}_s$ in Q_3 is calculated at t_1 directly. The variation of state fidelity $\mathcal{F}_s$ with the coupling strength g_{31} is presented in Fig. 6(c). It is revealed that the two groups have a similar trend of $\mathcal{F}_s$ while changing the g_{31}. In the strong coupling regime ($g > \max\{\gamma, \kappa\}$), the energy tends to oscillate between the transmon and memory qubit [10]. With increasing of the coupling strength, the interaction between the transmon and memory qubit may become too strong, and therefore too much dissipation would be generated in the system. In the group with memory operation (red scatter dots), a state fidelity of $\mathcal{F}_s \in [99.075\%, 99.625\%]$ is achieved by setting up $g_{31}/\omega_1 \in [0.001, 0.01]$, as marked by the gray range in Fig. 6(c). According to the above discussion, a suitable range of coupling strength is highlighted with the red shaded area in Figs. 6(b) and 6(c), where $g_{31}/2\pi \in [24, 39]$ MHz, the operation time $\Delta t \in [5, 10]$ ns, and the fidelity $\mathcal{F}_s \in [99.075\%, 99.435\%]$.

It should be noted that, when storing in the memory qubit, the connection of the memory qubit to the transmons can induce the fluctuation of the state fidelity. This characteristic can be manifested by utilizing the median fidelity $\overline{\mathcal{F}}_s$ and the fluctuation of fidelity $\Delta \mathcal{F}_s$:

$$\overline{\mathcal{F}}_s = \left(\mathcal{F}_s^{\max} + \mathcal{F}_s^{\min}\right)/2, \tag{14}$$

$$\Delta \mathcal{F}_s = \mathcal{F}_s^{\max} - \mathcal{F}_s^{\min}, \tag{15}$$

where $\mathcal{F}_s^{\max}$ ($\mathcal{F}_s^{\min}$) is the maximum (minimum) fidelity during the period from $t_1 = \pi/2g_{31}$ ns to a reasonable later time, say, $t_2 = \pi/2g_{31} + 20$ ns. Actually, at time t_2, the memory operation has been essentially completed, and the state fidelity embarks on a stage of fluctuations.

To mitigate this problem, a phase shift θ between the two coupling strength g_{31} and g_{41} is introduced. The interaction between transmons and the memory qubit becomes as [58–60]

$$\hat{H}_I' = g_{31}e^{i\theta}\hat{\sigma}_3^+\hat{a}_1 + g_{41}\hat{\sigma}_4^+\hat{a}_1 + \text{H.c.}, \tag{16}$$

where $g_{31} = g_{41} = 24 \times 2\pi$ MHz, $\theta \in [-\pi, \pi]$. Figures 7(a) and 7(b) give the state fidelity $\mathcal{F}_s$ in the memory qubit for $\theta = 0$ and $\theta = \pi$, respectively. The median fidelity and fluctuation of fidelity in the memory qubit are demonstrated in Figs. 7(c) and 7(d). The points marked by two solid blue rectangular boxes are corresponding to the data in Fig. 7(a), while two dashed green rectangular boxes highlight the data in Fig. 7(b). It can be seen that when θ is changed from 0 to $\pm\pi$, the median fidelity $\overline{\mathcal{F}}_s$ is improved by about 0.265%, and the fluctuation of fidelity $\Delta\mathcal{F}_s$ is reduced nearly by half.

For simplicity, the coupling strength between the transmon and memory qubit is set up as $g_m = 24 \times 2\pi$ MHz without considering the phase shift in the following subsections.

B. Disturbing effects

In the second case, some disturbing effects on the memory operations are studied, as illustrated by the ball-and-stick model in Fig. 8(a). Two transmons (Q_2 and Q_3) are coupled to the two memory qubits (M_2 and M_1) and the bus mode. The two transmons are excited and need to be stored into corresponding memory qubits with coupling strength $g_{31} = g_{23} = g_m$. In this situation, two outstanding disturbing effects are to be taken into account. The first is the coupling
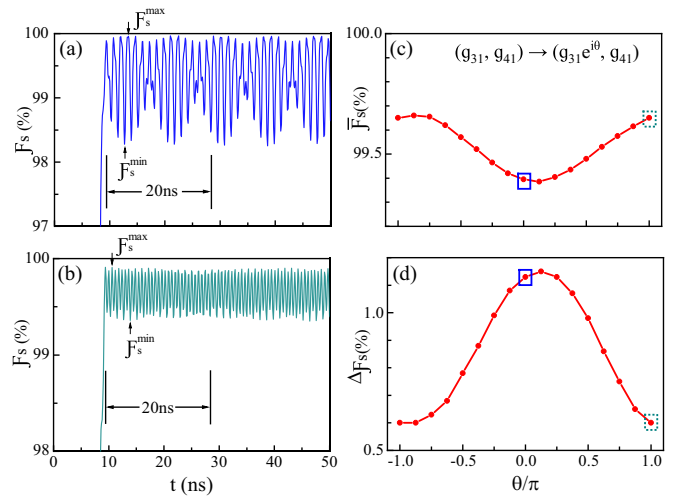

FIG. 7. Calculation results of Case I when introducing phase shift θ to the coupling strength g_{31}. (a) The median fidelity $\overline{\mathcal{F}}_s$ with different phase θ of coupling strength. (b) The fluctuation of fidelity $\Delta\mathcal{F}_s$ with different phase θ of coupling strength. (c) The state fidelity $\mathcal{F}_s$ in the memory qubit after a SWAP operation for $\theta = 0$. (d) The state fidelity $\mathcal{F}_s$ in the memory qubit after a SWAP operation for $\theta = \pi$. The fluctuation can be suppressed with the appropriate setup of the phase shift θ.

interaction between the transmon and bus mode with coupling strengths g_{22} and g_{32}. The other is an assumption that the memory mode leaks into other branches and is coupled to other transmons with coupling strengths g_{21} and g_{33}, which are indicated with irregular lines. Here, for convenience of calculation, disturbing effects of $g_{22} = g_b$ and $g_{21} = g_l$ are scrutinized for the storage of Q_2 to M_2, while for the storage of Q_3 to M_1, one assigns $g_{32} = g_b$ and $g_{33} = g_l$.

The Hamiltonian of the subsystem in Case II can be written as

$$\hat{H}_{CII} = \frac{1}{2}\left(\Omega_2\hat{\sigma}_2^z + \Omega_3\hat{\sigma}_3^z\right) + \sum_{j=1}^{3}\omega_j\hat{a}_j^\dagger\hat{a}_j$$

$$+ \sum_{i=2}^{3}\sum_{j=1}^{3}g_{ij}(\hat{\sigma}_i^+\hat{a}_j + \text{H.c.}). \tag{17}$$

The two transmons are excited at $\Omega_2 = 3.1 \times 2\pi$ GHz and $\Omega_3 = 3.2 \times 2\pi$ GHz. The storage from two transmons to the two memory qubits starts from $t_0 = 0$ ns to $t_1 = \pi/2g_m$ ns.

The photon numbers in the two memories M_1 and M_2 are $n_1 = \langle\hat{a}_1^\dagger\hat{a}_1\rangle$ and $n_3 = \langle\hat{a}_3^\dagger\hat{a}_3\rangle$, respectively. Then the two kinds of disturbing effects are demonstrated with the median photon number $\overline{n}$ and the fluctuation of photon number Δn in the memory qubits:

$$\overline{n} = (n_{\max} + n_{\min})/2, \tag{18}$$

$$\Delta n = n_{\max} - n_{\min}, \tag{19}$$

where $n_{\max}$ ($n_{\min}$) is the maximum (minimum) photon number in the memory qubit during the period from $t_1 = \pi/2g_m$ ns to a reasonable later time $t_2 = \pi/2g_m + 20$ ns, as mentioned similarly in the last subsection.
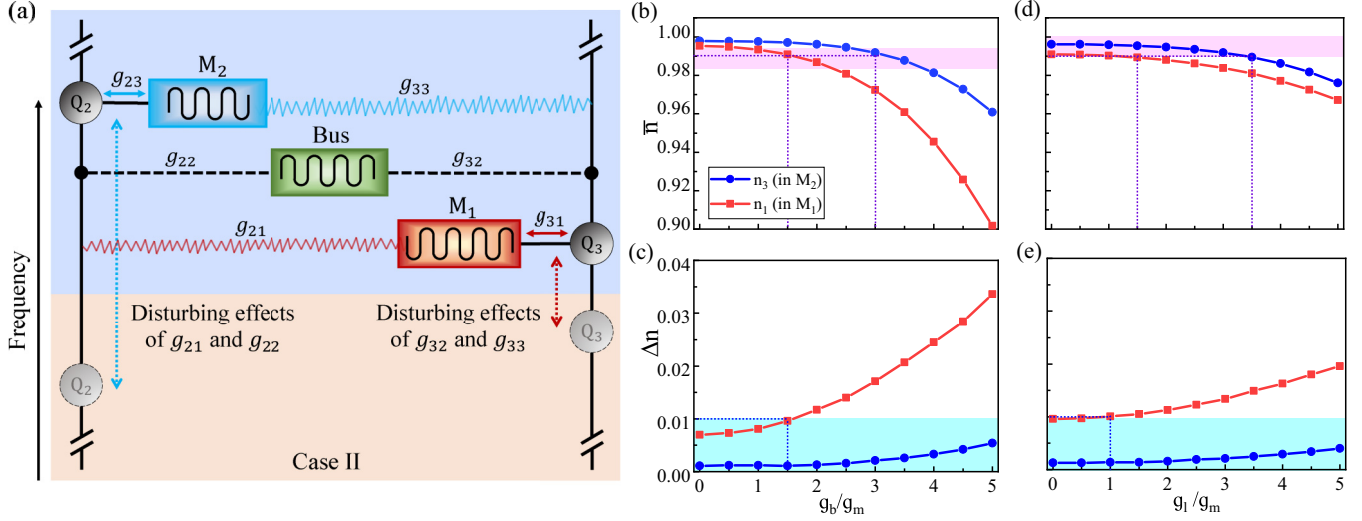
FIG. 8. Model and calculation results of Case II. (a) Ball-and-stick model for Case II: the disturbing effects of the coupling strength g_{21} and g_{22} (g_{33} and g_{32}) on the memory operation between Q_2 and M_2 (Q_3 and M_1), where g_{21} (g_{33}) indicated with irregular red bottom (blue upper) line is a disturbing coupling strength between Q_2 and M_1 (Q_3 and M_2). (b) The median photon number $\bar{n}$ in the memory qubit as a function of the ratio g_b/g_m. (c) The fluctuation of photon number Δn in the memory qubit as a function of the ratio g_b/g_m. (d) The median photon number $\bar{n}$ in the memory qubit as a function of the ratio g_1/g_m. (e) The fluctuation of photon number Δn in the memory qubit as a function of the ratio g_1/g_m. In (b)–(e) the line with blue circles is the photon number n_3 in M_2, and the line with red squares is the photon number n_1 in M_1.

For the first disturbing effect, which is caused by the coupling interaction between the transmon and bus mode, the median photon number $\bar{n}$ in the memory qubit is plotted as a function of the ratio g_b/g_m, as depicted in Fig. 8(b). The magenta upper area marks a range of $\bar{n}$, $0.99 \leqslant \bar{n} \leqslant 1$, which corresponds to $g_b/g_m \leqslant 1.5$ for M_1 and $g_b/g_m \leqslant 3$ for M_2, respectively. In Fig. 8(c) the fluctuations of the photon number in the two memory qubits are shown. The cyan bottom area refers to $\Delta n \leqslant 0.01$. In the following calculations, the coupling strength between Q_2 and the bus channel is $g_{22} = 2g_m$; the coupling strength between Q_3 and the bus channel is $g_{32} = 1.5g_m$.

For the second disturbing effect, which is caused by the possible leakage from memory mode to the other transmon, the median photon number $\bar{n}$ and the fluctuation of photon number Δn are plotted as functions of the ratio g_1/g_m in Figs. 8(d) and 8(e), respectively. The shaded area in Fig. 8(d) refers to the $0.99 \leqslant n \leqslant 1$, and the cyan bottom area in Fig. 8(e) is the $\Delta n \leqslant 0.01$. As mentioned in Sec. II, scattering parameter of the leakage mode is 80 dB less than the memory mode, which is negligible compared to the strong coupling strength g_m. Therefore, the effect of g_1 is ignored in the following discussions.

According to the above calculations, it is revealed that for the two kinds of disturbing effects, the memory operation from Q_3 to M_1 is more sensitive than that from Q_2 to M_2. The reason can be ascribed to the different frequency detuning among the three resonant modes, taken into account of the fact that the detuning of M_2 is larger than that of M_1 from the bus mode.

C. Coupling operation

In the last two subsections, the proper range of different coupling strengths has been defined, which provide the

storage speed, fidelity, and stability of the quantum memory. Taking these parameters into Case III, a coupling operation between Q_2 and Q_3 is constructed as displayed in Fig. 9(a). The Hamiltonian in this case can be written as

$$\hat{H}_{CIII} = \frac{1}{2}\left(\Omega_2\hat{\sigma}_2^z + \Omega_3\hat{\sigma}_3^z\right) + \sum_{j=1}^{3}\omega_j\hat{a}_j^\dagger\hat{a}_j$$
$$+ \left(g_{22}\hat{\sigma}_2^+\hat{a}_2 + g_{23}\hat{\sigma}_2^+\hat{a}_3 + \text{H.c.}\right)$$
$$+ \left(g_{31}\hat{\sigma}_3^+\hat{a}_1 + g_{32}\hat{\sigma}_3^+\hat{a}_2 + \text{H.c.}\right), \quad (20)$$

where the coupling strength $g_{23} = g_{31} = 24 \times 2\pi$ MHz, $g_{22} = 2g_{23}$, and $g_{32} = 1.5g_{31}$ are adopted in the following analysis.

In Figs. 9(b) and 9(c), the qubit excited state population $P_2 = \langle\sigma_2^+\sigma_2^-\rangle$ and $P_3 = \langle\sigma_3^+\sigma_3^-\rangle$ in the two transmons Q_2 (dashed blue line) and Q_3 (solid orange line) are calculated during the process of coupling operation via the bus mode. The transmon Q_2 is excited at the beginning, and the frequencies Ω_2 and Ω_3 are tuned to be resonant. Then the energy is exchanged between Q_2 and Q_3. It can be seen that, for $\Omega_2 = \Omega_3 = 3.0 \times 2\pi$ GHz, the iSWAP gate is finished at 267.1 ns with $P_3 = 0.979$ in Q_3, as shown in Fig. 9(b). Similarly for $\Omega_2 = \Omega_3 = 5.5 \times 2\pi$ GHz in Fig. 9(c), the iSWAP gate is finished at 92.2 ns with $P_3 = 0.988$ in Q_3. The operation time is determined by the coupling strength between Q_2 and Q_3 via the bus channel, which is adjustable by tuning the detuning from the tranmsons to the bus mode [52]. The high-frequency oscillations in the curves of Fig. 9(c) can be ascribed to the small detuning between the transmons and bus mode [61].

D. Entangled state storage

Up to now, both the memory operation and coupling operation have been discussed for the multimode circuit QED system. In the fourth case, an entangled state is studied to
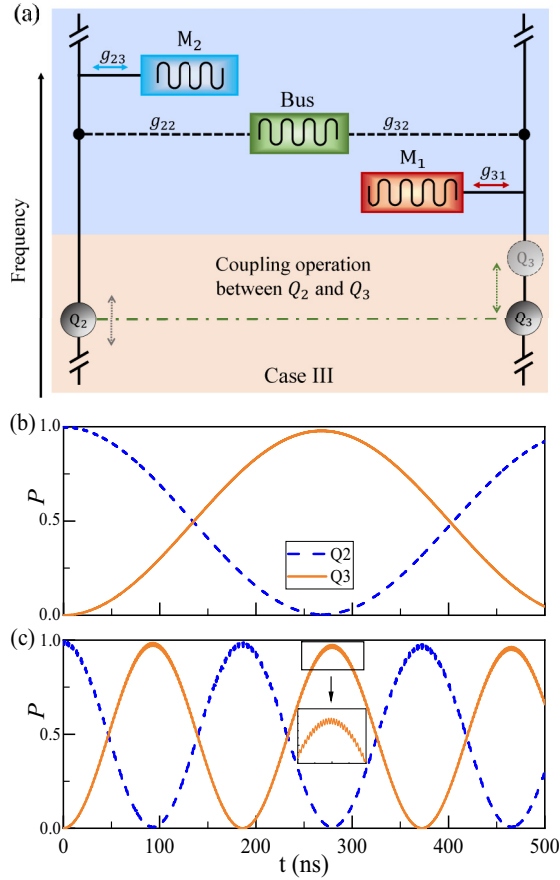
FIG. 9. Model and calculation results of Case III. (a) Ball-and-stick model for Case III: coupling operation between Q_2 and Q_3. (b) Energy is exchanged between Q_2 (dashed blue line) and Q_3 (solid orange line) when $\Omega_2 = \Omega_3 = 3.0 \times 2\pi$ GHz. (c) Energy is exchanged between Q_2 (dashed blue line) and Q_3 (solid orange line) when $\Omega_2 = \Omega_3 = 5.5 \times 2\pi$ GHz. The inset is an enlarged segment of the curve to emphasize the high-frequency oscillations of P.
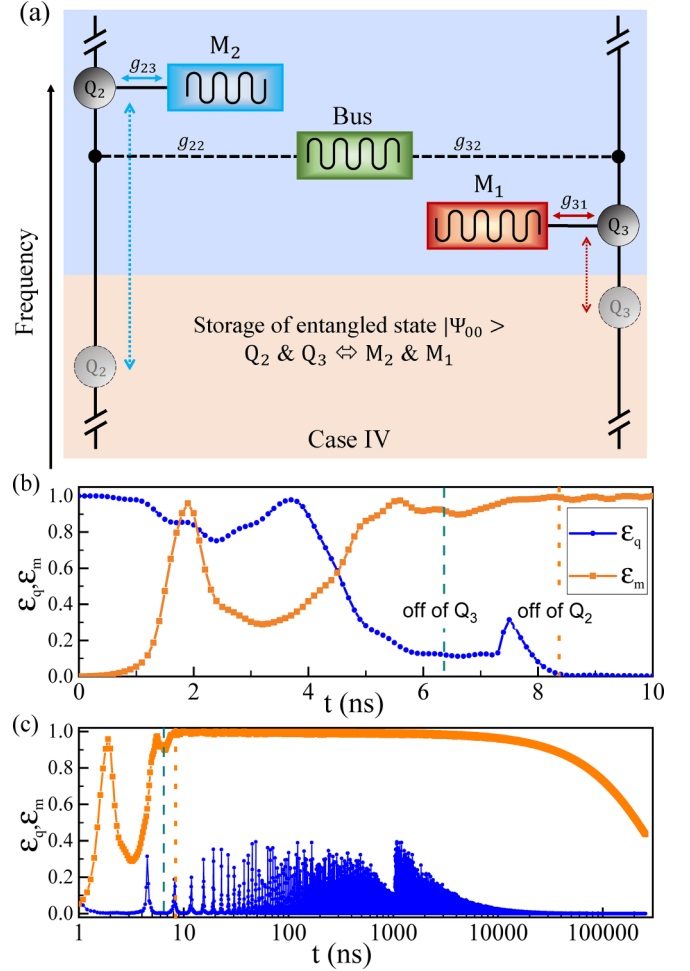

FIG. 10. Model and calculation results of Case IV. (a) Ball-and-stick model for Case IV: storage of the entangled state $|\Psi_{00}\rangle = (|00\rangle + |11\rangle)/\sqrt{2}$ from Q_2 and Q_3 to M_2 and M_1. (b) The entanglement in the memory qubits $\mathcal{E}_m$ (line with orange squares) and in the transmons $\mathcal{E}_q$ (line with blue circles); the storage off time of transmons Q_2 and Q_3 is tuned for higher fidelity of the two memory operations. (c) The retention of the entanglement in the memory qubits.

see the feasibility of entangled state storage in two memory qubits. As depicted in Fig. 10(a), two transmons Q_2 and Q_3 are prepared in a Bell state $|\Psi_{00}\rangle = (|00\rangle + |11\rangle)/\sqrt{2}$. Then the quantum information is stored in two memory qubits M_2 and M_1. The entanglement in the transmons is calculated according to the logarithmic negativity [62], which is defined as

$$\mathcal{E}_q(\rho_q) = \log_2 \left\| \rho_q^{T_{Q_2}} \right\|_1, \tag{21}$$

where ρ_q is the reduced density matrix of the two transmons, and $||\rho_q^{T_{Q_2}}||_1$ is the trace norm of ρ_q with respect to Q_2. Similarly, the entanglement in the two memory qubits is defined by

$$\mathcal{E}_m(\rho_m) = \log_2 \left\| \rho_m^{T_{M_1}} \right\|_1, \tag{22}$$

where ρ_m is the reduced density matrix of the two memory qubits, and $||\rho_m^{T_{M_1}}||_1$ is the trace norm of ρ_m with respect to M_1.

The storage of the entangled state in the two transmons requires two memory operations. The first is between Q_2 and

M_2, the other is between Q_3 and M_1. Setting up the two operations starts at $t_0 = 0$ ns, and the entanglements in the memory qubits $\mathcal{E}_m$ (line with orange squares) and the transmons $\mathcal{E}_q$ (line with blue circles) are calculated along with time, as shown in Fig. 10(b). Even though the entanglement curve $\mathcal{E}_m$ experiences some fluctuations during the process of memory operations, it can be stabilized at 0.999 within 10 ns. Correspondingly, the entanglement curve $\mathcal{E}_q$ decreases to zero in a manner roughly complementary to $\mathcal{E}_m$. It can be seen in Fig. 10(c) that the entanglement in the memory qubits $\mathcal{E}_m$ decreases with time because of decoherence, while the entanglement in the transmon qubits $\mathcal{E}_q$ would have some clear fluctuations before diminishing to zero. Therefore it is imperative to reset the transmon qubits to the ground state before the information retrieval.

TABLE II. Comparisons of some quantum memories.

Theor./ exp.[a]	System	Encoding	Storage/ retrieval	Operation time	Coupling strength (MHz)	Storage fidelity(%)	Storage time	Auxiliary element	Extra module[b]	Ref.
Exp.	NV center	—	Both	—	0.0044	—	$T_1(20.8\,\text{ns})$, $T_2(175\,\text{ns})$	—	$D\ (\approx 1\,\mu\text{m})$	[19]
Exp.	Magnetic particle	—	—	—	—	—	5 ks (30 K), 7 ks (20 K)	—	270 nm	[21]
Exp.	3D cavity	FS[c]	Both	—	1	99	T_1 (1.22 ms), T_2 (0.72 ms)	Readout cavity	$V\ (\geqslant 1\ \text{cm}^3)$	[22]
Exp.	3D cavity	—	—	—	50–120	—	$\geqslant 2$ ms	Iris	$L(20\ \text{cm})$, $W(4.6\ \text{cm})$, $H(6\ \text{cm})$	[23]
Exp.	CPW	—	Storage	—	20	—	T_1 (5μs), $T_2 \approx 2T_1$	None	L (4.5–4.65 mm)	[24]
Exp.	CPW	CS[d]	Both	—	0.25–0.86	—	0.51 μs	None	$L\ (\geqslant 1\ \text{cm})$	[17]
Theor.	NV center	—	Both	10 ns	35	97.5	T_1 (1 ms), T_2 (0.01 ms)	—	$L\ (\geqslant 10\ \mu\text{m})$	[18]
Theor.	NV center	—	Both	—	0.35–0.7	$\geqslant 90$	10 ms	YIG[e]	μm scale	[20]
Theor.	CPW	—	Both	74.1 ps	56	—	950 μs	JJ-FET[f]	$L\ (\geqslant 1\ \text{mm})$	[25]
Theor.	CPW	FS	Both	10 ns	24	99.4	1 ms	None	None	This work

[a]Theor.: theory; Exp.: experiment.
[b]About the size of extra module, L: length; W: width; H: height, D: depth, V: volume.
[c]FS: Fock state.
[d]CS: Coherent state.
[e]YIG: Yttrium iron garnet.
[f]JJ-FET: Josephson field effect transistors.

V. DISCUSSION

We have studied the properties of the specially designed multimode circuit QED system, including storage speed, fidelity, and stability, for the application to a quantum memory in the superconducting quantum processor. Some other issues about the quantum memory should also be discussed here.

The interaction between the transmon and bus mode is closely correlated to the control pulse on the transmon when it is near-resonant with the memory qubit. In the above cases, the control pulses on the transmons are set as an ideal square wave. The high-frequency components in the square wave might induce unwanted excitation of transmons. Therefore, the Gaussian or rising cosine waveform is generally adopted in practical experiments [63,64]. Further improvements of storage efficiency in practical operations can be realized by optimizing the waveform in controlling superconducting qubits [63] and enhancing the quality factor of resonant modes in CPW resonators [10,32,65,66].

The retrieval of information from the memory qubit can be realized by a similar SWAP operation to a storage process. However, one pitfall must be taken care of. Before the retrieval operation, the transmon qubit should be reset to the ground state $|0\rangle$ to ensure the memory qubit being refreshed to $|0\rangle$ rather than being contaminated by the unknown state in the transmon. The physical reason behind such a requirement is the no-cloning theorem for quantum information. To reset the quantum state of transmon, an all-microwave method can be utilized [67]. This reset process would be achieved within 0.5 μs with 0.2% residual excitation.

In this work, CPWs with four branches are researched for detailed calculations about the characteristics of quantum memory. For a superconducting quantum processor with a larger number of qubits, it is possible to enlarge the number of branches of the multimode cavity to contain more memory qubits. Higher complexity would be generated with more resonant modes, which would put higher demands on the precise operations of these resonant modes.

To compare the scheme in this work with other memory protocols for quantum information processing, different kinds of quantum memory are listed in Table II. It can be seen that many kinds of physical systems can be used as the quantum memory for quantum computation. The 3D cavity and CPW are two typical examples in circuit QED systems, which can have strong coupling with the superconducting qubits [17,22–25]. Due to the planar layout, the CPW system has more advantages in the smaller size, better connectivity, and higher scalability than that of the 3D cavity. Since more CPW resonators used in the quantum memory would increase the total size of the quantum processor, this work presents a proposal that could miniaturize the quantum memory by combining the memory qubits with a specially designed multimode bus cavity without any other auxiliary elements.

As for the encoding protocol, Fock states can be utilized to construct logical qubits $|0_L\rangle$ and $|1_L\rangle$. In this work, the first two Fock states $\{|0\rangle, |1\rangle\}$ are directly used for quantum information storage. This encoding protocol has an advantage of lower rate of photon decay compared to other encoding protocols which involve higher Fock states $|n\rangle$, $n \geqslant 2$ [10,68].

VI. CONCLUSIONS

In summary, the multimode cavity with specially designed CPW resonators is proposed to serve as a promising candidate for constructing a miniaturized quantum memory. By capacitive coupling to the superconducting transmon qubits, the CPW multimode resonators with multiple branches are able to integrate the bus modes and memory modes without introducing any other ancillary parts, thus reducing the total size of the quantum processor. The key feature of the quantum memory modes is that the current distribution is localized, which is especially beneficial to the access of the information in transmons without suffering crosstalks from other resonant modes. Decoherence time of the quantum processor can be prolonged more than one order of magnitude longer than that without quantum memory.

Frequencies of qubits and a suitable range of distinct coupling strengths used in the system are analyzed for higher selectivity of every resonant mode. By solving the master equation for the evolution of corresponding subsystem density operators, it has been found that the coupling strength between the transmon and memory qubit should satisfy $g_m/2\pi \in [24, 40]$ MHz, where the operation time of the memory storage can be in $\Delta t \in [5, 10]$ ns with state fidelity $\mathcal{F}_s \in [99.075\%, 99.435\%]$. The coupling strength g_b between the bus mode and the transmon is related to the frequency detuning among these resonant modes in the multimode cavity, while the leakage from the other memory mode is ignored for a relatively weak signal strength. In addition, two transmons are taken as a pair of typical example for the realization of coupling operation via the bus channel and storage of entangled states. The multimode circuit QED system with a miniaturized quantum memory shows potential in prolonging the decoherence time of a superconducting quantum processor and sheds light on an exciting approach towards large-scale superconducting quantum computing.

[1] M. H. Devoret, J. M. Martinis, and J. Clarke, Measurements of Macroscopic Quantum Tunneling Out of the Zero-Voltage State of a Current-Biased Josephson Junction, Phys. Rev. Lett. **55**, 1908 (1985).

[2] Y. Nakamura, C. D. Chen, and J. S. Tsai, Spectroscopy of Energy-Level Splitting between Two Macroscopic Quantum States of Charge Coherently Superposed by Josephson Coupling, Phys. Rev. Lett. **79**, 2328 (1997).

[3] A. Wallraff, D. I. Schuster, A. Blais, L. Frunzio, R. S. Huang, J. Majer, S. Kumar, S. M. Girvin, and R. J. Schoelkopf, Strong coupling of a single photon to a superconducting qubit using circuit quantum electrodynamics, Nature (London) **431**, 162 (2004).

[4] J. Q. You and F. Nori, Atomic physics and quantum optics using superconducting circuits, Nature (London) **474**, 589 (2011).

[5] O. Kyriienko and A. S. Sørensen, Floquet Quantum Simulation with Superconducting Qubits, Phys. Rev. Appl. **9**, 064029 (2018).

[6] F. Arute, K. Arya, R. Babbush, D. Bacon, J. C. Bardin, R. Barends, R. Biswas, S. Boixo, F. G. S. L. Brandao, D. A. Buell *et al.*, Quantum supremacy using a programmable superconducting processor, Nature (London) **574**, 505 (2019).

[7] S. A. Wilkinson and M. J. Hartmann, Superconducting quantum many-body circuits for quantum simulation and computing, Appl. Phys. Lett. **116**, 230501 (2020).

[8] Z. J. Chen, K. J. Satzinger, J. Atalaya, A. N. Korotkov, A. Dunsworth, D. Sank, C. Quintana, M. McEwen, R. Barends, P. V. Klimov *et al.*, Exponential suppression of bit or phase errors with cyclic error correction, Nature (London) **595**, 600 (2021).

[9] Y. L. Wu, W. S. Bao, S. R. Cao, F. S. Chen, M. C. Chen, X. W. Chen, T. H. Chung, H. Deng, Y. J. Du, D. J. Fan *et al.*, Strong Quantum Computational Advantage using a Superconducting Quantum Processor, Phys. Rev. Lett. **127**, 180501 (2021).

[10] A. Blais, A. L. Grimsmo, S. M. Girvin, and A. Wallraff, Circuit quantum electrodynamics, Rev. Mod. Phys. **93**, 025005 (2021).

[11] R. K. Naik, N. Leung, S. Chakram, P. Groszkowski, Y. Lu, N. Earnest, D. C. McKay, J. Koch, and D. I. Schuster, Random access quantum information processors using multimode circuit quantum electrodynamics, Nat. Commun. **8**, 1904 (2017).

[12] A. P. M. Place, L. V. H. Rodgers, P. Mundada, B. M. Smitham, M. Fitzpatrick, Z. Q. Leng, A. Premkumar, J. Bryon, A. Vrajitoarea, S. Sussman *et al.*, New material platform for superconducting transmon qubits with coherence times exceeding 0.3 milliseconds, Nat. Commun. **12**, 1779 (2021).

[13] C. L. Wang, X. G. Li, H. K. Xu, Z. Y. Li, J. H. Wang, Z. Yang, Z. Y. Mi, X. H. Liang, T. Su, C. H. Yang *et al.*, Towards practical quantum computers: transmon qubit with a lifetime approaching 0.5 milliseconds, NPJ Quantum Inform. **8**, 3 (2022).

[14] B. T. H. Varcoe, S. Brattke, M. Weidinger, and H. Walther, Preparing pure photon number states of the radiation field, Nature (London) **403**, 743 (2000).

[15] H. J. Kimble, The quantum internet, Nature (London) **453**, 1023 (2008).

[16] K. S. Chou, J. Z. Blumoff, C. S. Wang, P. C. Reinhold, C. J. Axline, Y. Y. Gao, L. Frunzio, M. H. Devoret, L. Jiang, and R. J. Schoelkopf, Deterministic teleportation of a quantum gate between two logical qubits, Nature (London) **561**, 368 (2018).

[17] Z. H. Bao, Z. L. Wang, Y. K. Wu, Y. Li, C. Ma, Y. P. Song, H. Y. Zhang, and L. M. Duan, On-Demand Storage and Retrieval of Microwave Photons Using a Superconducting Multiresonator Quantum Memory, Phys. Rev. Lett. **127**, 010503 (2021).

[18] X. Y. Lü, Z. L. Xiang, W. Cui, J. Q. You, and F. Nori. Quantum memory using a hybrid circuit with flux qubits and nitrogen-vacancy centers, Phys. Rev. A **88**, 012329 (2013).

[19] S. Saito, X. B. Zhu, R. Amsüss, Y. Matsuzaki, K. Kakuyanagi, T. Shimo-Oka, N. Mizuochi, K. Nemoto, W. J. Munro, and K. Semba, Towards Realizing a Quantum Memory for a

Superconducting Qubit: Storage and Retrieval of Quantum States, Phys. Rev. Lett. **111**, 107008 (2013).

[20] Y. Y. Lai, G. D. Lin, J. Twamley, and H. S. Goan, Single-nitrogen-vacancy-center quantum memory for a superconducting flux qubit mediated by a ferromagnet, Phys. Rev. A **97**, 052303 (2018).

[21] K. Konwar, S. D. Kaushik, D. Sen, and P. Deb, Dynamic spin freezing and magnetic memory effect in ensembles of interacting anisotropic magnetic nanoparticles, Phys. Rev. B **102**, 174449 (2020).

[22] M. Reagor, W. Pfaff, C. Axline, R. W. Heeres, N. Ofek, K. Sliwa, E. Holland, C. Wang, J. Blumoff, K. Chou *et al.*, Quantum memory with millisecond coherence in circuit QED, Phys. Rev. B **94**, 014506 (2016).

[23] T. H. Jang, J. Lee, J. Shin, J. Kang, S. Han, I. Jeon, S. Chakram, D. I. Schuster, and H. Kwon, Mode-manipulated multimode cavity for quantum memory, IEEE Trans. Quantum Eng. **3**, 3102610 (2022).

[24] E. A. Lucero, Computing prime factors using a Josephson phase-qubit architecture: $15 = 3 \times 5$, Ph.D. thesis, Univ. California (2012).

[25] K. Sardashti, M. C. Dartiailh, J. Yuan, S. Hart, P. Gumann, and J. Shabani, Voltage-tunable superconducting resonators: A platform for random access quantum memory, IEEE Trans. Quantum Eng. **1**, 5502107 (2020).

[26] S. Kuhr, S. Gleyzes, C. Guerlin, J. Bernu, U. B. Hoff, S. Deléglise, S. Osnaghi, M. Brune, J. M. Raimond, S. Haroche, E. Jacques, P. Bosland, and B. Visentin, Ultrahigh finesse Fabry-Pérot superconducting resonator, Appl. Phys. Lett. **90**, 164101 (2007).

[27] H. Paik, D. I. Schuster, L. S. Bishop, G. Kirchmair, G. Catelani, A. P. Sears, B. R. Johnson, M. J. Reagor, L. Frunzio, L. I. Glazman *et al.*, Observation of High Coherence in Josephson Junction Qubits Measured in a Three-Dimensional Circuit QED Architecture, Phys. Rev. Lett. **107**, 240501 (2011).

[28] M. Mirrahimi, Z. Leghtas, V. V. Albert, S. Touzard, R. J. Schoelkopf, L. Jiang, and M. H. Devoret, Dynamically protected cat-qubits: A new paradigm for universal quantum computation, New J. Phys. **16**, 045014 (2014).

[29] J. M. Sage, V. Bolkhovsky, W. D. Oliver, B. Turek, and P. B. Welander, Study of loss in superconducting coplanar waveguide resonators, J. Appl. Phys. **109**, 063915 (2011).

[30] M. J. Reagor, Superconducting Cavities for circuit quantum electrodynamics, Ph.D. thesis, Yale University (2015).

[31] M. Göppl, A. Fragner, M. Baur, R. Bianchetti, S. Filipp, J. M. Fink, P. J. Leek, G. Puebla, L. Steffen, and A. Wallraff, Coplanar waveguide resonators for circuit quantum electrodynamics, J. Appl. Phys. **104**, 113904 (2008).

[32] G. Calusine, A. Melville, W. Woods, R. Das, C. Stull, V. Bolkhovsky, D. Braje, D. Hover, D. K. Kim, X. Miloshi *et al.*, Analysis and mitigation of interface losses in trenched superconducting coplanar waveguide resonators, Appl. Phys. Lett. **112**, 062601 (2018).

[33] S. Chakram, A. E. Oriani, R. K. Naik, A. V. Dixit, K. He, A. Agrawal, H. Kwon, and D. I. Schuster, Seamless High-Q Microwave Cavities for Multimode Circuit Quantum Electrodynamics, Phys. Rev. Lett. **127**, 107701 (2021).

[34] D. I. Schuster, A. A. Houck, J. A. Schreier, A. Wallraff, J. M. Gambetta, A. Blais, L. Frunzio, J. Majer, B. Johnson, M. H.

Devoret *et al.*, Resolving photon number states in a superconducting circuit, Nature (London) **445**, 515 (2007).

[35] J. Kerckhoff, K. Lalumière, B. J. Chapman, A. Blais, and K. W. Lehnert, On-Chip Superconducting Microwave Circulator from Synthetic Rotation, Phys. Rev. Appl. **4**, 034002 (2015).

[36] D. Maxwell, D. J. Szwer, D. Paredes-Barato, H. Busche, J. D. Pritchard, A. Gauguet, K. J. Weatherill, M. P. A. Jones, and C. S. Adams, Storage and Control of Optical Photons using Rydberg Polaritons, Phys. Rev. Lett. **110**, 103001 (2013).

[37] M. Pierre, I. Svensson, S. R. Sathyamoorthy, G. Johansson, and P. Delsing, Storage and on-demand release of microwaves using superconducting resonators with tunable coupling, Appl. Phys. Lett. **104**, 232604 (2014).

[38] T. Astner, S. Nevlacsil, N. Peterschofsky, A. Angerer, S. Rotter, S. Putz, J. Schmiedmayer, and J. Majer, Coherent Coupling of Remote Spin Ensembles via a Cavity Bus, Phys. Rev. Lett. **118**, 140502 (2017).

[39] G. Wendin, Quantum information processing with superconducting circuits: A review, Rep. Prog. Phys. **80**, 106001 (2017).

[40] S. Mahashabde, E. Otto, D. Montemurro, S. Graaf, S. Kubatkin, and A. Danilov, Fast Tunable High-Q-Factor Superconducting Microwave Resonators, Phys. Rev. Appl. **14**, 044040 (2020).

[41] B. Kannan, D. L. Campbell, F. Vasconcelos, R. Winik, D. K. Kim, M. Kjaergaard, P. Krantz, A. Melville, B. M. Niedzielski, J. L. Yoder *et al.*, Generating spatially entangled itinerant photons with waveguide quantum electrodynamics, Sci. Adv. **6**, eabb8780 (2020).

[42] M. Mirhosseini, A. Sipahigil, M. Kalaee, and O. Painter, Superconducting qubit to optical photon transduction, Nature (London) **588**, 599 (2020).

[43] C. Rigetti, J. M. Gambetta, S. Poletto, B. L. T. Plourde, J. M. Chow, A. D. Corcoles, J. A. Smolin, S. T. Merkel, J. R. Rozen, G. A. Keefe *et al.*, Superconducting qubit in a waveguide cavity with a coherence time approaching 0.1 ms, Phys. Rev. B **86**, 100506(R) (2012).

[44] C. Delacour, L. Ortega, M. Faucher, T. Crozes, T. Fournier, B. Pannetier, and V. Bouchiat, Persistence of superconductivity in niobium ultrathin films grown on R-plane sapphire, Phys. Rev. B **83**, 144504 (2011).

[45] A. A. Clerk, M. H. Devoret, S. M. Girvin, Florian Marquardt, and R. J. Schoelkopf, Introduction to quantum noise, measurement, and amplification, Rev. Mod. Phys. **82**, 1155 (2010).

[46] M. O. Scully and M. S. Zubairy, *Quantum Optics* (Cambridge University Press, Cambridge, 1997).

[47] A. Blais, R. S. Huang, A. Wallraff, S. M. Girvin, and R. J. Schoelkopf, Cavity quantum electrodynamics for superconducting electrical circuits: An architecture for quantum computation, Phys. Rev. A **69**, 062320 (2004).

[48] S. E. Rasmussen, K. S. Christensen, S. P. Pedersen, L. B. Kristensen, T. Bækkegaard, N. J. S. Loft, and N. T. Zinner, The Superconducting Circuit Companion—An Introduction with Worked Examples, PRX Quantum **2**, 040204 (2021).

[49] E. T. Jaynes and F. W. Cummings, Comparison of quantum and semiclassical radiation theories with application to the beam maser, Proc. IEEE **51**, 89 (1963).

[50] A. Blais, J. Gambetta, A. Wallraff, D. I. Schuster, S. M. Girvin, M. H. Devoret, and R. J. Schoelkopf, Quantum-information processing with circuit quantum electrodynamics, Phys. Rev. A **75**, 032329 (2007).

[51] M. Hofheinz, H. Wang, M. Ansmann, R. C. Bialczak, E. Lucero, M. Neeley, A. D. O'Connell, D. Sank, J. Wenner, and J. M. Martinis *et al.*, Synthesizing arbitrary quantum states in a superconducting resonator, Nature (London) **459**, 546 (2009).

[52] P. Krantz, M. Kjaergaard, F. Yan, T. P. Orlando, S. Gustavsson, and W. D. Oliver, A quantum engineer's guide to superconducting qubits, Appl. Phys. Rev. **6**, 021318 (2019).

[53] J. S. Kelly, Fault-tolerant superconducting qubits, Ph.D. thesis, Univ. California (2015).

[54] E. Lucero, R. Barends, Y. Chen, J. Kelly, M. Mariantoni, A. Megrant, P. O'Malley, D. Sank, A. Vainsencher, J. Wenner *et al.*, Computing prime factors with a Josephson phase qubit quantum processor, Nat. Phys. **8**, 719 (2012).

[55] R. Schack and T. A. Brun, AC++ library using quantum trajectories to solve quantum master equations, Comput. Phys. Commun. **102**, 210 (1997).

[56] C. N. Benlloch, Open systems dynamics: Simulating master equations in the computer, arXiv:1504.05266.

[57] Z. Puchała, Bound on trace distance based on superfidelity, Phys. Rev. A **79**, 024302 (2009).

[58] P. Bertet, C. J. P. M. Harmans, and J. E. Mooij, Parametric coupling for superconducting qubits, Phys. Rev. B **73**, 064512 (2006).

[59] A. A. Clerk, Introduction to quantum non-reciprocal interactions: From non-Hermitian Hamiltonians to quantum master equations and quantum feedforward schemes, SciPost Phys. Lect. Notes 44 (2022).

[60] B. Peropadre, D. Zueco, F. Wulschner, F. Deppe, A. Marx, R. Gross, and J. José Garcia-Ripoll, Tunable coupling engineering between superconducting resonators: From sidebands to effective gauge fields, Phys. Rev. B **87**, 134504 (2013).

[61] C. Song, K. Xu, W. Liu, C. P. Yang, S. B. Zheng, H. Deng, Q. Xie, K. Huang, Q. Guo, L. Zhang *et al.*, 10-Qubit Entanglement and Parallel Logic Operations with a Superconducting Circuit, Phys. Rev. Lett. **119**, 180511 (2017).

[62] G. Vidal and R. F. Werner, Computable measure of entanglement, Phys. Rev. A **65**, 032314 (2002).

[63] L. B. Nguyen, G. Koolstra, Y. Kim, A. Morvan, T. Chistolini, S. Singh, K. N. Nesterov, C. Jünger, L. Chen, Zahra Pedramrazi *et al.*, Blueprint for a High-Performance Fluxonium Quantum Processor, PRX Quantum **3**, 037001 (2022).

[64] J. C. Bardin, D. H. Slichter, and D. J. Reilly, Microwaves in quantum computing, IEEE J. Microw. **1**, 403 (2021).

[65] A. Bruno, G. de Lange, S. Asaad, K. L. van der Enden, N. K. Langford, and L. DiCarlo, Reducing intrinsic loss in superconducting resonators by surface treatment and deep etching of silicon substrates, Appl. Phys. Lett. **106**, 182601 (2015).

[66] C. Wang, C. Axline, Y. Y. Gao, T. Brecht, Y. Chu, L. Frunzio, M. H. Devoret, and R. J. Schoelkopf, Surface participation and dielectric loss in superconducting qubits, Appl. Phys. Lett. **107**, 162601 (2015).

[67] P. Magnard, P. Kurpiers, B. Royer, T. Walter, J.-C. Besse, and S. Gasparinetti, Fast and Unconditional All-Microwave Reset of a Superconducting Qubit, Phys. Rev. Lett. **121**, 060502 (2018).

[68] M. H. Michael, M. Silveri, R. T. Brierley, V. V. Albert, J. Salmilehto, L. Jiang, and S. M. Girvin, New Class of Quantum Error-Correcting Codes for a Bosonic Mode, Phys. Rev. X **6**, 031006 (2016).